

Ultrafine Nickel-Nanoparticle-Enabled SiO₂ Hierarchical Hollow Spheres for High-Performance Lithium Storage

Chunjuan Tang, Yuning Liu, Chang Xu, Jiexin Zhu, Xiujuan Wei, Liang Zhou,* Liang He, Wei Yang, and Liqiang Mai*

The high theoretical capacity and natural abundance of SiO₂ make it a promising high-capacity anode material for lithium-ion batteries. However, its widespread application is significantly hampered by the intrinsic poor electronic conductivity and drastic volume variation. Herein, a unique hollow structured Ni/SiO₂ nanocomposite constructed by ultrafine Ni nanoparticle (≈3 nm) functionalized SiO₂ nanosheets is designed. The Ni nanoparticles boost not only the electronic conductivity but also the electrochemical activity of SiO₂ effectively. Meanwhile, the hollow cavity provides sufficient free space to accommodate the volume change of SiO₂ during repeated lithiation/delithiation; the nanosheet building blocks reduce the diffusion lengths of lithium ions. Due to the synergistic effect between Ni and SiO₂, the Ni/SiO₂ composite delivers a high reversible capacity of 676 mA h g⁻¹ at 0.1 A g⁻¹. At a high current density of 10 A g⁻¹, a capacity of 337 mA h g⁻¹ can be retained after 1000 cycles.

materials, silicon (Si) has the highest theoretical capacity (4200 mA h g⁻¹).^[16] However, the synthesis of Si-based nanostructures is usually complicated and costly.^[17–21] In addition, the capacity of Si fades rapidly with cycling due to the drastic volume variation (about 400%).^[22]

Silica (SiO₂) is one of the most abundant materials on the earth and it has a high theoretical specific capacity of 1965 mA h g⁻¹.^[23–25] Gao et al. first reported that nanosized silica has electrochemical activity toward lithium.^[26] Since then, SiO₂ has been considered as a promising substitute for Si.^[23,27] Nevertheless, SiO₂ also suffers large volume change and low intrinsic electronic conductivity, which lead to unsatisfactory electrochemical performance.

To enhance the electrochemical performance of SiO₂, several strategies have been proposed. One effective approach is designing SiO₂ hollow structures for volume change accommodation.^[23,24,28] The other strategy is compositing SiO₂ with carbonaceous materials to improve the electronic conductivity.^[29–32] Besides carbonaceous materials, metals can also be used to boost the electronic conductivity of active materials.^[33–36] For example, Jo and co-workers reported the fabrication of conifer-like hierarchical SiO_x/NiSi_x with enhanced structural stability and kinetics.^[34] However, to the best of our knowledge, SiO₂/metal based anode materials have been rarely reported.

In this work, a facile in situ reduction approach has been demonstrated to fabricate ultrafine nickel nanoparticle (≈3 nm) functionalized SiO₂ hierarchical hollow spheres (Ni/SiO₂). With ultrafine Ni nanoparticles embedded in the amorphous SiO₂ matrix, the resulting Ni/SiO₂ nanocomposite delivers a high reversible capacity of 676 mA h g⁻¹ at 0.1 A g⁻¹. A specific capacity of 337 mA h g⁻¹ can be achieved after 1000 cycles at a high current density of 10 A g⁻¹.

1. Introduction

Lithium-ion batteries (LIBs) have been widely employed in portable electronics. To extend their applications in hybrid electric vehicles and electric vehicles, LIBs with higher energy density and power density are in demand.^[1–3] The theoretical capacity of commercial graphite is only 372 mA h g⁻¹, which significantly limits the energy density of LIBs. Thus, various alternative anode materials with higher capacities have been developed, such as Si,^[4–7] Sn,^[8–10] and metal oxides.^[11–15] Among these

Prof. C. J. Tang, Y. N. Liu, C. Xu, J. X. Zhu, X. J. Wei, Prof. L. Zhou, Prof. L. He, W. Yang, Prof. L. Q. Mai
State Key Laboratory of Advanced Technology for Materials Synthesis and Processing
International School of Materials Science and Engineering
Wuhan University of Technology
Wuhan 430070, P. R. China
E-mail: liangzhou@whut.edu.cn; mlq518@whut.edu.cn

Prof. C. J. Tang
Department of Mathematics and Physics
Luoyang Institute of Science and Technology
Luoyang 471023, P. R. China

Prof. L. Q. Mai
Department of Chemistry
University of California
Berkeley, CA 94720, USA

 The ORCID identification number(s) for the author(s) of this article can be found under <https://doi.org/10.1002/adfm.201704561>.

DOI: 10.1002/adfm.201704561

2. Results and Discussion

The preparation of Ni-functionalized SiO₂ hierarchical hollow spheres (Ni/SiO₂) includes two steps (**Figure 1a**). In step I, nickel silicate hierarchical hollow spheres are synthesized by hydrothermal treating of Stöber SiO₂ spheres in the presence of nickel (II) ions. In step II, the nickel silicate hierarchical hollow spheres are in situ converted into Ni/SiO₂ hierarchical hollow

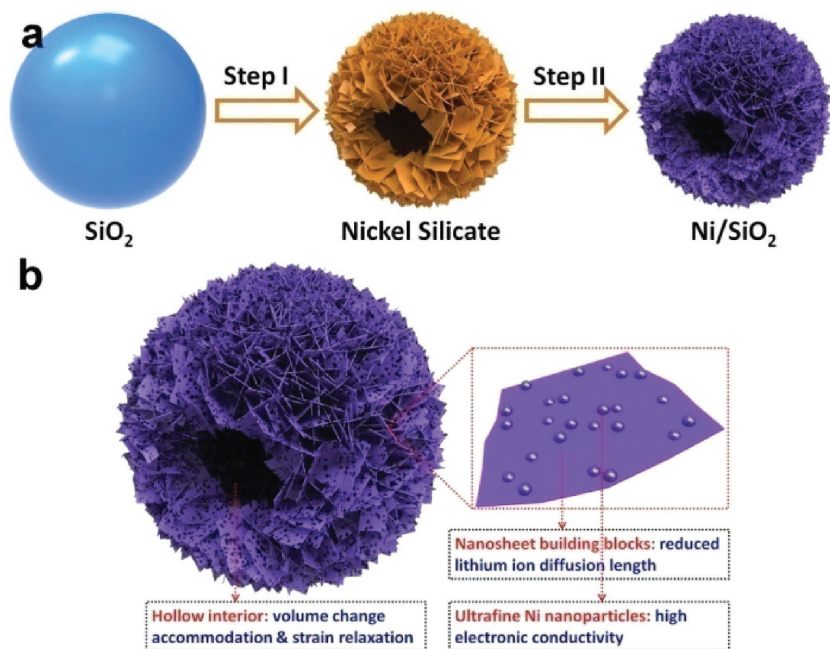


Figure 1. a) Schematic illustration for the synthesis of Ni/SiO₂ hierarchical hollow spheres. Step I: hydrothermal treatment of Stöber SiO₂ spheres; Step II: annealing the nickel silicate in H₂/Ar (5%/95%). b) Schematic illustration of a detailed Ni/SiO₂ hierarchical hollow sphere.

spheres by annealing in H₂/Ar at an elevated temperature. The obtained Ni/SiO₂ composite has the following structural features (Figure 1b): (I) the sample has a microspherical morphology with a hollow cavity at the center; (II) the microspheres are constructed by nanosheet building blocks (the so-called hierarchical structure); and (III) each SiO₂ nanosheet building block is decorated with numerous ultrafine Ni nanoparticles.

The intermediate, nickel silicate, shows a uniform spherical morphology with a narrow size distribution (Figure S1, Supporting Information). The average size of the spheres is around 500 nm. From high-magnification scanning electron microscope (SEM) image (Figure S1b, Supporting Information), one can know that the nickel silicate spheres are actually constructed by numerous interconnected nanosheet building blocks. The hollow cavity can be clearly discerned from the broken spheres (Figure S1b, Supporting Information) and transmission electron microscopy (TEM) image (Figure S2, Supporting Information).

After annealing the nickel silicate in H₂/Ar at elevated temperatures, Ni/SiO₂ composites can be obtained. The morphology and microstructure of a typical sample, Ni/SiO₂-550, are shown in Figure 2. The Ni/SiO₂-550 is composed of monodisperse microspheres with sizes of ≈500 nm (Figure 2a,b). Just like the nickel silicate intermediate, the Ni/SiO₂-550 spheres are also constructed by interconnected nanosheets, forming a hierarchical structure. The hollow cavity can be clearly observed at the broken sites of the spheres. TEM image further confirms the hierarchical hollow structure of the Ni/SiO₂-550 (Figure 2c,d). The selected area electron diffraction (SAED) pattern of Ni/SiO₂-550 shows a series of concentric diffraction rings, demonstrating the polycrystalline feature of Ni/SiO₂-550 (Figure 2e). From inside to outside, the rings can be indexed to the (111), (200), (220), and (222) diffractions of Ni.

Under high-resolution transmission electron microscopy (HRTEM) image, it is observed that ultrafine Ni nanoparticles (≈3 nm) bestrew homogeneously in the amorphous silica matrix; the (111) lattice fringes of Ni with interplanar distance of 0.21 nm can be clearly observed (Figure 2f). Elemental mapping results shown in Figure 2g demonstrate the uniform distribution of Ni, Si, and O in the Ni/SiO₂-550. The Ni/Si molar ratio of Ni/SiO₂-550 is determined to be 1.485:1 by inductive coupled plasma (ICP) and the SiO₂ weight percentage is calculated to be 40.65% (Table S1, Supporting Information).

The morphology and structure of Ni/SiO₂-600, Ni/SiO₂-650, and Ni/SiO₂-700 are shown in Figure 3. All the samples exhibit a hierarchical hollow spherical morphology with narrow size distribution, which is similar to that of Ni/SiO₂-550. The Ni nanoparticles grow with the increase of annealing temperature. From HRTEM images, the sizes of Ni nanoparticles for Ni/SiO₂-600, Ni/SiO₂-650, and Ni/SiO₂-700 are determined to be 5–7, 8–10, and 10–18 nm, respectively.

X-ray diffractometer (XRD) patterns of the samples prepared at different temperatures

are presented in Figure 4a. The broad peak at ≈20° indicates the presence of amorphous SiO₂. The peaks located at 44.36°, 51.90°, and 76.30° can be indexed to the (111), (200), and (220) diffractions of cubic Ni (JCPDS no. 01-070-1849). In general, the crystallinity of the Ni nanoparticles enhances with the increase of annealing temperature, which can be deduced from intensity of the diffraction peaks. Meanwhile, the diffraction peaks sharpen with the increase of temperature, suggesting the increase in crystallite size. The average crystallite sizes of the Ni nanoparticles are calculated by Scherrer equation. The average crystallite sizes of Ni for Ni/SiO₂-550, Ni/SiO₂-600, Ni/SiO₂-650, and Ni/SiO₂-700 are determined to be 2.5, 5.7, 9.2, and 15 nm, respectively. If the annealing temperature is lowered to 500 °C, the nickel silicate cannot be converted into Ni/SiO₂ nanocomposite thoroughly (Figure S3, Supporting Information).

The chemical states of Ni and Si in Ni/SiO₂-550 are identified by X-ray photoelectron spectroscopy (XPS). The Ni 2p core-level spectrum exhibits two main peaks at 852.1 and 869.8 eV, corresponding the 2p_{3/2} and 2p_{1/2} peaks of Ni(0) (Figure 4b), respectively. Two obvious satellite peaks can also be observed at 857.8 and 876.0 eV (Figure 4b).^[37] The Si 2p_{3/2} peak is observed at 103.6 eV, which is characteristic for Si(IV) (Figure 4c). The XPS results confirm that the product is composed of elementary Ni and SiO₂. The textural property of the Ni/SiO₂ is studied by N₂ sorption (Figure 4d). The Ni/SiO₂-550 exhibits a specific Brunauer-Emmett-Teller (BET) surface area of 244 m² g⁻¹. With the increase of annealing temperature, the BET surface areas decrease monotonously (Table S2, Supporting Information).

To investigate the electrochemical performances of Ni/SiO₂ composites, coin cells are assembled using Ni/SiO₂ as the working electrode and lithium chips as the counter electrode. Figure S4 in the Supporting information shows the CV curves

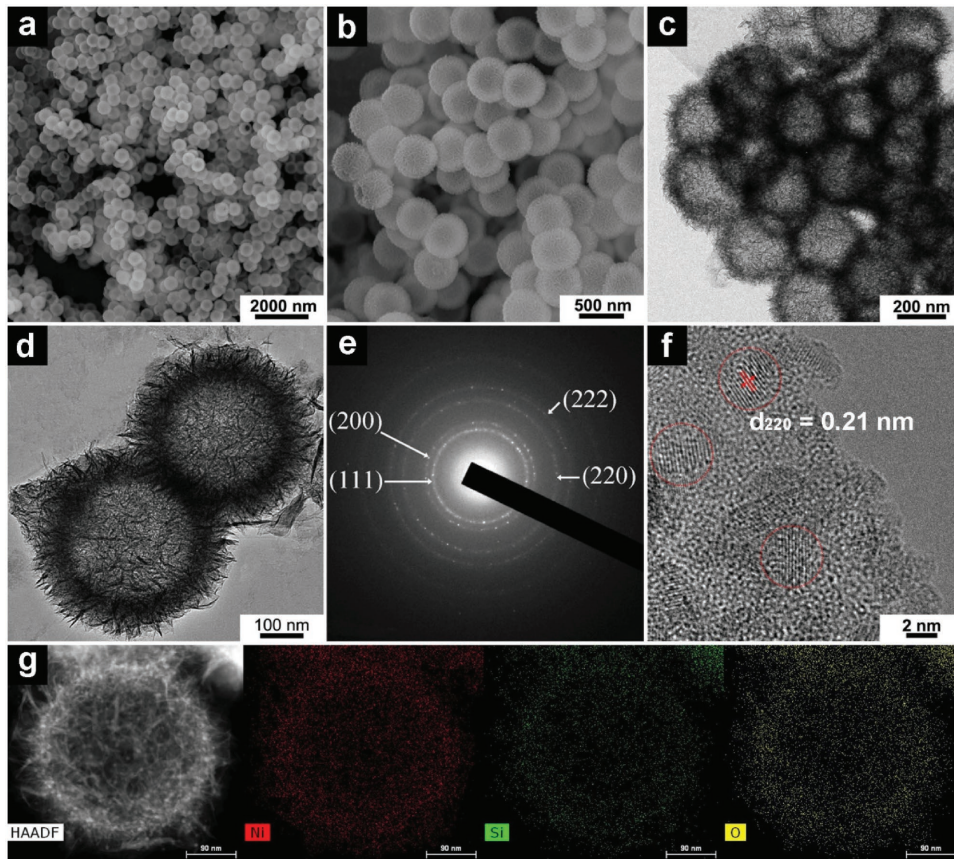


Figure 2. a,b) SEM images, c,d) TEM images, e) SAED pattern, f) HRTEM image, and g) elemental mapping results of Ni/SiO₂-550.

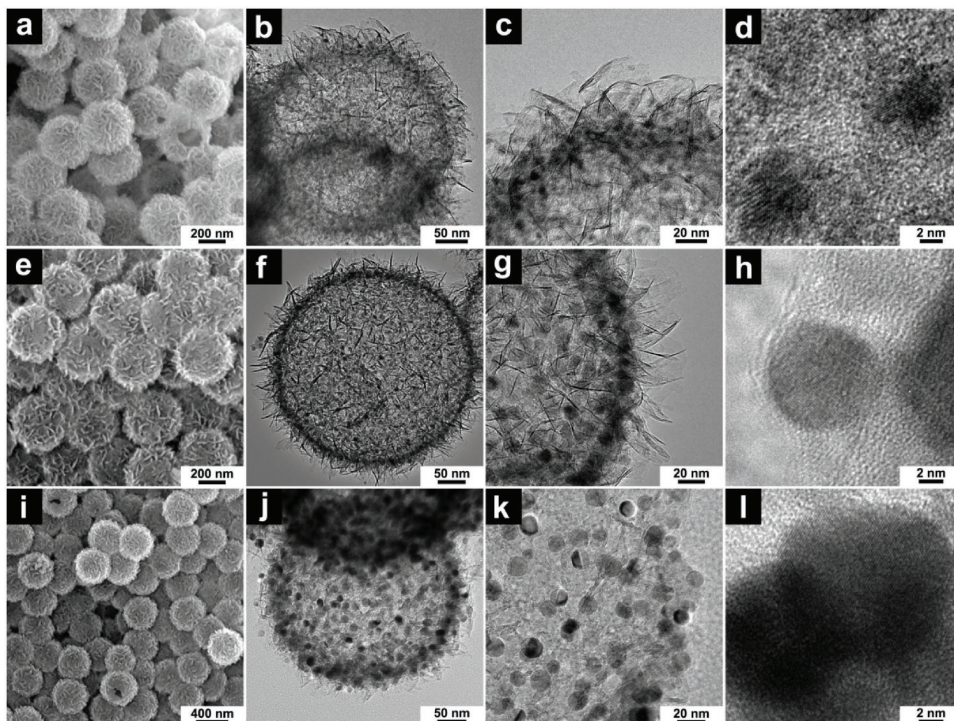


Figure 3. a–d) SEM, TEM, and HRTEM images of Ni/SiO₂-600, e–h) Ni/SiO₂-650, and i–l) Ni/SiO₂-700.

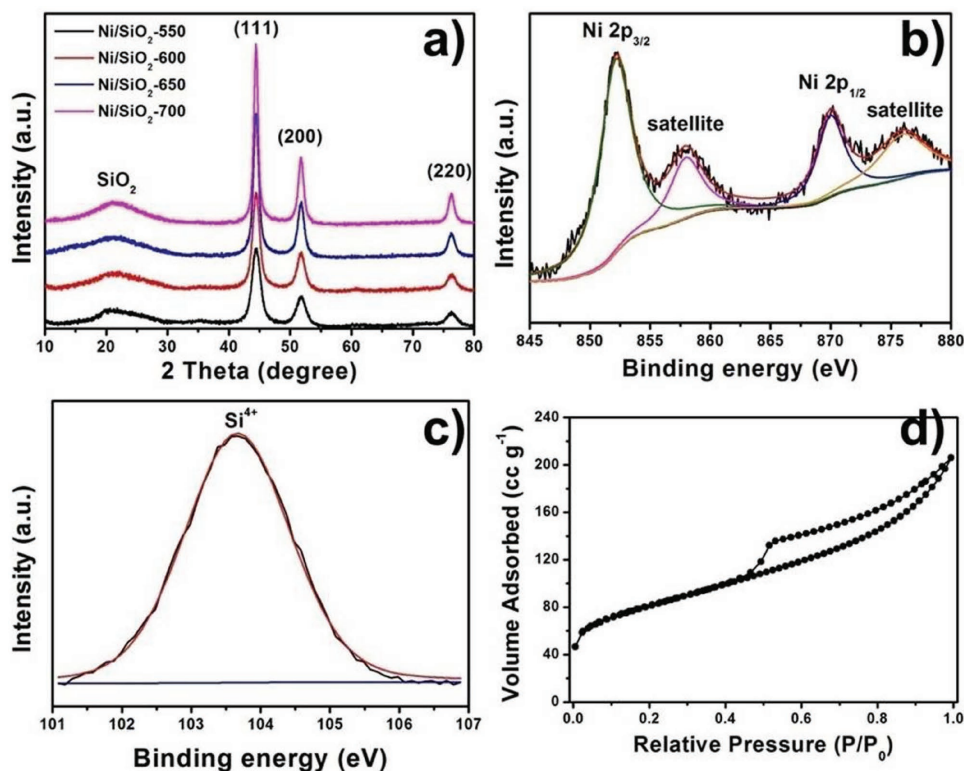


Figure 4. a) XRD patterns of the Ni/SiO₂ composites prepared at different temperatures, b) Ni 2p spectrum, and c) Si 2p spectrum and N₂ adsorption-desorption isotherm of Ni/SiO₂-550.

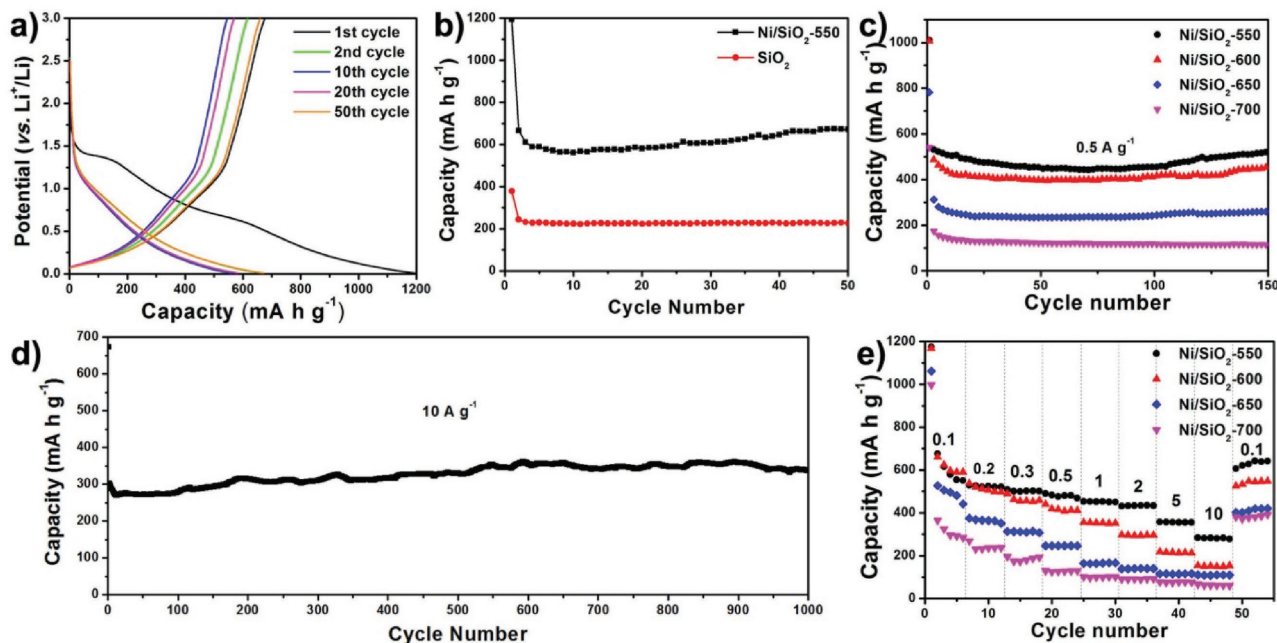


Figure 5. Electrochemical performances of the Ni/SiO₂ nanocomposites and pristine SiO₂. a) Representative discharge/charge curves of Ni/SiO₂-550 at 0.1 A g⁻¹; b) cycling performance of Ni/SiO₂-550 and pristine SiO₂ at 0.1 A g⁻¹; c) cycling performances of Ni/SiO₂ nanocomposites at 0.5 A g⁻¹; d) cycling performance of Ni/SiO₂-550 at 10 A g⁻¹; and e) rate performances of Ni/SiO₂ nanocomposites.

of Ni/SiO₂-550 in the potential range of 0.01–3.0 V at a scan rate of 0.05 mV s⁻¹. There are three reduction peaks in the first cathodic scan. The broad peak located at ≈1.4 V can be ascribed to the reactions between SiO₂ and lithium (5SiO₂ + 4Li⁺ + 4e⁻ → 2Li₂Si₂O₅ + Si; 2SiO₂ + 4Li⁺ + 4e⁻ → Li₄SiO₄ + Si; SiO₂ + 4Li⁺ + 4e⁻ → 2Li₂O + Si).^[27] The broad peak at ≈0.65 V is ascribed to electrolyte decomposition and the formation of a solid electrolyte interphase (SEI) layer.^[27,28] Both broad peaks disappear in the subsequent cycles. The third cathodic peak at ≈0 V can be assigned to the alloying reaction between Si and lithium (Si + xLi⁺ + x e⁻ → Li_xSi).^[38] In the first charge process, an obvious peak appears at 0.15 V, which is ascribed to dealloying of Li_xSi.^[24] For the subsequent cycles, the CV curves overlap, suggesting the highly reversible reaction between lithium and the in situ generated Si.

Figure 5a depicts selected discharge/charge curves of Ni/SiO₂-550 at 0.1 A g⁻¹. There are two pronounced plateaus at around 0.65 and 1.4 V in the first discharge curve, which disappear in the following discharge curves. The discharge curves agree well with the CV profiles. Figure 5b presents the cycling performance of the Ni/SiO₂-550 at 0.1 A g⁻¹. The initial discharge and charge capacities are 1195 and 676 mA h g⁻¹, respectively. The irreversible capacity can be attributed to the formation of SEI layer and the irreversible electrochemical reaction between lithium and SiO₂. The initial coulombic efficiency (56.6%) is relatively low for practical applications, and this issue could be solved by prelithiation.^[39] The discharge capacity decreases from 666 mA h g⁻¹ for the second cycle to 561 mA h g⁻¹ for the 10th cycle and then increases slightly. After 50 cycles, a high discharge capacity of 672 mA h g⁻¹ can be obtained. For comparison, pristine SiO₂ hierarchical hollow spheres are also prepared (Figure S5, Supporting Information). Although the pristine SiO₂ hollow spheres show a similar morphology to Ni/SiO₂-550, they deliver a much lower reversible capacity, which is only ≈240 mA h g⁻¹ at the current density of 0.1 A g⁻¹ (Figure 5b). The result demonstrates that the ultrafine Ni nanoparticles can boost the electrochemical activity of SiO₂.

The cycling performances of the Ni/SiO₂ nanocomposites prepared at different temperatures at 0.5 A g⁻¹ are shown in Figure 5c. Generally, all the samples show good cycling stability; the lower the annealing temperature is, the higher the reversible capacity. The Ni/SiO₂-550 delivers a discharge capacity of 522 mA h g⁻¹ after 150 cycles, which is much higher than those of Ni/SiO₂-600 (455 mA h g⁻¹), Ni/SiO₂-650 (260 mA h g⁻¹), and Ni/SiO₂-700 (114 mA h g⁻¹). Besides, the initial coulombic efficiency of Ni/SiO₂-550 (54%) is higher than those of Ni/SiO₂-600 (51.7%), Ni/SiO₂-650 (44.9%), and Ni/SiO₂-700 (35.6%). The volumetric capacity represents another important parameter for practical use. The Ni/SiO₂-550 demonstrates a stable volumetric capacity of ≈450 mA h cm⁻³ (Figure S6, Supporting Information).

Figure S7 (Supporting information) and Figure 5d present the high-rate cycling performance of Ni/SiO₂-550. At a current density of 2 A g⁻¹, the initial discharge and charge capacities are 928 and 527 mA h g⁻¹, respectively (Figure S7, Supporting Information). The discharge capacity increases slowly in the first 200 cycles and then stabilizes; the capacity increase upon cycling could be attributed to the reversible formation/dissolution of a polymeric gel-like film.^[40,41] After 600 cycles, a

stable discharge capacity of 730 mA h g⁻¹ is obtained. Under the same current density, the capacity of Ni/SiO₂-500 decays to 47.5 mA h g⁻¹ after 100 cycles (Figure S8, Supporting Information). At an ultrahigh current density of 10 A g⁻¹, a capacity of 337 mA h g⁻¹ can be retained after 1000 cycles, indicating the excellent cycling stability of Ni/SiO₂-550 (Figure 5d).

To further evaluate the electrochemical properties, rate performances of the samples prepared at different temperatures and the pristine SiO₂ are presented in Figure 5e and Figure S9 (Supporting information). The Ni/SiO₂-550 shows the highest specific capacity and best rate capability. It delivers discharge capacities of 551 (the 6th cycle), 521, 502, 469, 450, 434, 356, and 278 mA h g⁻¹ at current densities of 0.1, 0.2, 0.3, 0.5, 1, 2, 5, and 10 A g⁻¹, respectively. When the current density is returned to 0.1 A g⁻¹, a high discharge capacity of 642 mA h g⁻¹ can be recovered.

To understand the difference in lithium storage performance among the samples, electrochemical impedance spectroscopy (EIS) is conducted in the frequency range of 0.01 to 100 kHz (Figure S10, Supporting Information). The charge transfer resistance (*R*_{ct}) of the electrodes can be determined from the size of the depressed semicircle in the medium-frequency region. The *R*_{ct} value of Ni/SiO₂-550 is determined to be 61.4 Ω, which is smaller than that of Ni/SiO₂-600 (99.9 Ω), Ni/SiO₂-650 (171.5 Ω), Ni/SiO₂-700 (200.3 Ω), and pristine SiO₂ (273.0 Ω). The results demonstrate that the Ni nanoparticles enhance the conductivity of the nanocomposite; the smaller the Ni nanoparticle is, the better the conductivity is. The low-frequency sloping line is ascribed to Warburg impedance, associated with the diffusion of Li⁺ in the bulk of the electrode material. The Li⁺ diffusion coefficient *D* can be calculated from the sloping lines using the following equation^[42]

$$D = R^2 T^2 / 2 A^2 n^4 F^4 C^2 \sigma^2 \quad (1)$$

In this equation, *R* is the gas constant, *T* is the absolute temperature, *A* is the surface area of the electrode, *n* is the number of electrons per molecule during oxidation, *F* is the Faraday constant, *C* is the Li⁺ concentration with the value of 7.69 × 10⁻³ mol cm⁻³, and *σ* is the Warburg factor associated with *Z'* (*Z'* ∝ *σω*^{-1/2}). The linear fitting between *Z'* and *ω*^{-1/2} is shown in Figure S11 in the Supporting information. The estimated Warburg factor values of Ni/SiO₂-550, Ni/SiO₂-600, Ni/SiO₂-650, Ni/SiO₂-700, and pristine SiO₂ are 23.5, 324.3, 733.5, 1709.6, and 2578.1, respectively. The corresponding Li⁺ diffusion coefficient *D* calculated from Equation (1) is 1.12 × 10⁻¹⁴, 5.88 × 10⁻¹⁷, 1.15 × 10⁻¹⁷, 2.12 × 10⁻¹⁸, and 9.31 × 10⁻¹⁹ cm² s⁻¹, respectively. The Ni/SiO₂-550 shows the largest Li⁺ diffusion coefficient.

EIS of the Ni/SiO₂-550 after different cycle numbers is shown in Figure S12 in the Supporting information. No obvious change in *R*_{ct} can be observed, suggesting the good structural stability of Ni/SiO₂-550 and the formation of a stable SEI layer. Ex situ SEM and TEM images of the Ni/SiO₂-550 after 100 cycles at 0.1 A g⁻¹ (in discharged state) are shown in Figure S13 in the Supporting information. The hollow microspherical structure of Ni/SiO₂-550 can be well maintained after cycling. No obvious active material pulverization or structural collapse can be observed (Figure S13a–c, Supporting Information).

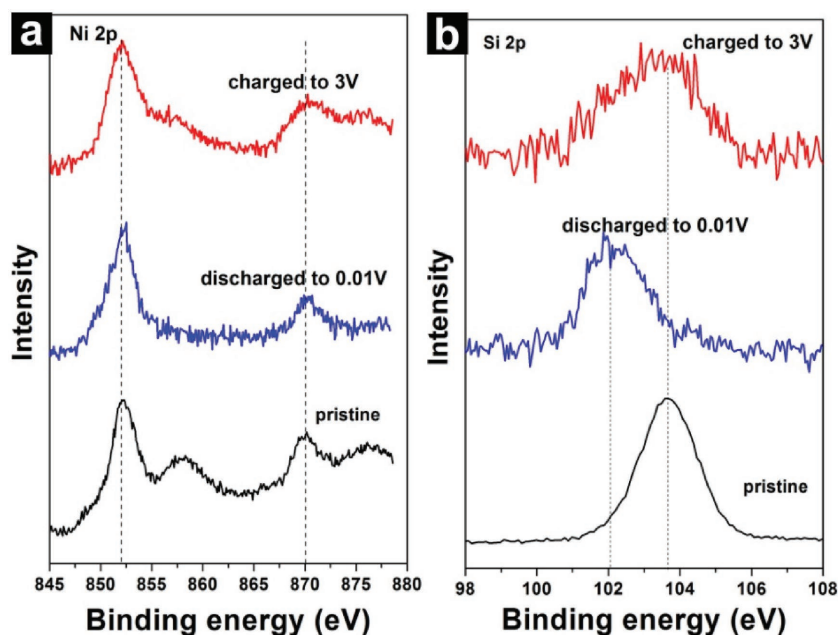
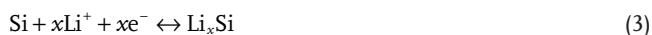
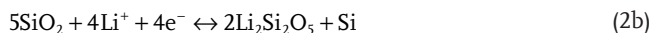


Figure 6. a) Ni 2p and b) Si 2p XPS spectra of Ni/SiO₂-550 at different states.

Notably, even the ultrafine Ni nanoparticles can be retained (indicated by white circles in Figure S13d in the Supporting information). The ex situ SEM and TEM results further confirm the excellent structural stability of Ni/SiO₂-550.

Ex situ XPS is employed to investigate the chemical state change of Ni/SiO₂-550 during discharge/charge. The major peaks for Ni do not change with cycling, indicating the Ni does not change in valence state (Figure 6a). On sharp contrast, the Si 2p_{3/2} peak shifts from 103.7 to 102.0 eV during discharge, suggesting the reduction of Si(VI) to Li_xSi (Figure 6b).^[23,25] When charged to 3 V, the peak shifts back to its original position.

According to literatures, the reactions between SiO₂ and lithium can be summarized as follows^[23,27]



The reactions (2a), (2b), and (2c) happen in parallel and are competing. The Si is electrochemically active, while the Li₂O, Li₂Si₂O₅, and Li₄SiO₄ are electrochemically inactive. The reaction (2a) can yield more Si and thus higher capacity than the other two reactions. It has been proposed that fine SiO₂ nanoparticles prefer the formation of Si via reaction (2a).^[25] The Ni/SiO₂ hierarchical hollow spheres are composed of ultrathin Ni/SiO₂ nanosheets, making the reaction mainly proceed through reaction (2a). As a result, a high specific capacity can be achieved.

The Ni/SiO₂-550 delivers a reversible capacity of 676 mA h g⁻¹ at 0.1 A g⁻¹. Considering the weight percentage of SiO₂ in the composite (40.65%), the reversible capacity of SiO₂ reaches 1663 mA h g⁻¹.

It is well known that the SiO₂ is an electronic insulator. The poor electronic conductivity and large volume expansion during lithiation are two major factors limiting the lithium storage performance of SiO₂. In the constructed nanocomposite, the ultrafine Ni nanoparticles are embedded in the SiO₂ matrix homogeneously, forming an electron highway. With enhanced electronic conductivity, the electrochemical activity and rate capability of SiO₂ are significantly boosted. The hollow cavity of Ni/SiO₂-550 provides sufficient free space for volume change accommodation and strain relaxation, boosting the structural stability and cycling stability. In addition, the nanosheet building blocks of Ni/SiO₂-550 provide short-ion diffusion lengths, benefiting to the rate capability.

3. Conclusion

Ultrafine Ni nanoparticle decorated SiO₂ hierarchical hollow spheres are successfully synthesized by a facile in situ reduction method. The ultrafine Ni nanoparticles (≈3 nm) enable the SiO₂ hierarchical hollow structure excellent lithium storage performance. The Ni/SiO₂-550 delivers a high specific capacity of 676 mA h g⁻¹ at 0.1 A g⁻¹. A capacity of 337 mA h g⁻¹ can be achieved after 1000 cycles at an ultrahigh current density of 10 A g⁻¹. The finding of this work demonstrates the fabrication of metal/SiO₂ nanocomposites as a promising means to boost the performance of SiO₂ for lithium storage.

4. Experimental Section

Synthesis of Ni-Nanoparticle-Functionalized SiO₂ Hierarchical Hollow Spheres: Nickel silicate (Ni₃Si₂O₅(OH)₄) hierarchical hollow spheres were synthesized according to the literature.^[43] To obtain Ni/SiO₂, the nickel silicate hollow spheres were heated in H₂/Ar (5%/95%) at different temperatures for 10 h with a temperature ramping rate of 2 °C min⁻¹. The samples prepared at 500, 550, 600, 650, and 700 °C are denoted as Ni/SiO₂-500, Ni/SiO₂-550, Ni/SiO₂-600, Ni/SiO₂-650, and Ni/SiO₂-700, respectively. The pristine SiO₂ hierarchical hollow spheres were obtained by etching the nickel from nickel silicate hierarchical hollow spheres selectively with 1.0 M HCl at 60 °C for 12 h.

Characterization: The crystalline structure of the samples was characterized by D8 Advance XRD with a nonmonochromated Cu Kα X-ray source. The morphology and microstructure of the samples were characterized with field emission-scanning electron microscopy (JEOL-7100F) and transmission electron microscopy (JEM-2100F). BET surface areas were calculated from nitrogen adsorption-desorption isotherms measured at 77 K using a Tristar II 3020 instrument. XPS analysis was conducted on a VG Multilab 2000. The Ni/Si ratio was determined by ICP.

Electrochemical Performance: 2016-type coin cells were assembled in a glove box filled with Ar. Lithium chips were used as the counter

electrode and reference electrode. The working electrode was obtained by mixing the active material, acetylene black, and carboxyl methyl cellulose in a weight ratio of 70:25:5. The slurry was casted on copper foil and dried in a vacuum oven. The mass loading of the active material was 1.0–1.3 mg cm⁻². The electrolyte was 1.0 M LiPF₆ in the mixture of ethylene carbonate and dimethyl carbonate with a volume ratio of 1:1. The cells were placed at ambient temperature for at least 2 h before the electrochemical performance test. Galvanostatic discharge/charge measurements were performed at a potential range of 0.01–3.0 V versus Li⁺/Li using a multichannel battery testing system (LAND CT2001A). Cyclic voltammetry (CV) and EIS were tested by electrochemical workstations (Autolab Potentiostat Galvanostat 302N and CHI760D).

Supporting Information

Supporting Information is available from the Wiley Online Library or from the author.

Acknowledgements

C.J.T and Y.N.L contributed equally to this work. This work was supported by the National Key Research Program of China (Grant No. 2016YFA0202603), the National Basic Research Program of China (Grant No. 2013CB934103), National Natural Science Foundation of China (Grant Nos. 61501215, 21673171, 51602239 and 51502226), the National Natural Science Fund for Distinguished Young Scholars (Grant No. 51425204), the Natural Science Foundation of Henan Province (Grant Nos. 17A430004, 152300410114, and 16A140012), the Program for Youth Scholar Teachers Supporting Plan in Universities of Henan province (Grant No. 2013GGJ5-189), the China Postdoctoral Science Foundation (Grant Nos. 2016M592401 and 2015T80845), and Fundamental Research Funds for WHUT Students Innovation and Entrepreneurship Training Program (Grant No. 20161049701002).

Conflict of Interest

The authors declare no conflict of interest.

Keywords

hollow spheres, lithium storage, nanocomposites, SiO₂, synergistic effects

Received: August 10, 2017

Revised: September 15, 2017

Published online:

- [1] N. Xu, T. Qian, X. J. Liu, J. Liu, Y. Chen, C. L. Yan, *Nano Lett.* **2017**, *17*, 538.
- [2] J. Liu, T. Qian, M. F. Wang, X. J. Liu, N. Xu, Y. Z. You, C. L. Yan, *Nano Lett.* **2017**, *17*, 5064.
- [3] W. Chen, T. Qian, J. Xiong, N. Xu, X. J. Liu, J. Liu, J. Q. Zhou, X. W. Shen, T. Z. Yang, Y. Chen, C. L. Yan, *Adv. Mater.* **2017**, *29*, 1605160.
- [4] Y. Jin, S. Li, A. Kushima, X. Q. Zheng, Y. M. Sun, J. Xie, J. Sun, W. J. Xue, G. M. Zhou, J. Wu, F. F. Shi, R. F. Zhang, Z. Zhu, K. So, Y. Cui, J. Li, *Energy Environ. Sci.* **2017**, *10*, 580.
- [5] J. Ryu, D. Hong, S. Choi, S. Park, *ACS Nano* **2016**, *10*, 2843.
- [6] N. Liu, H. Wu, M. T. McDowell, Y. Yao, C. Wang, Y. Cui, *Nano Lett.* **2012**, *12*, 3315.
- [7] N. Liu, Z. Lu, J. Zhao, M. T. McDowell, H. W. Lee, W. Zhao, Y. Cui, *Nat. Nanotechnol.* **2014**, *9*, 187.
- [8] J. Liu, Y. R. Wen, P. A. Aken, J. Maier, Y. Yu, *Nano Lett.* **2014**, *14*, 6387.
- [9] J. Hassoun, S. Panero, P. Simon, P. L. Taberna, B. Scrosati, *Adv. Mater.* **2007**, *19*, 1632.
- [10] K. Eom, J. Jung, J. T. Lee, V. Lair, T. Lair, *Nano Energy* **2015**, *12*, 314.
- [11] Q. Y. An, F. Lv, Q. Q. Liu, C. H. Han, K. N. Zhao, J. Z. Sheng, Q. L. Wei, M. Y. Yan, L. Q. Mai, *Nano Lett.* **2014**, *14*, 6250.
- [12] H. W. Zhang, L. Zhou, O. Noonan, D. J. Martin, A. K. Whittaker, C. Z. Yu, *Adv. Funct. Mater.* **2014**, *24*, 4337.
- [13] L. Zhang, K. N. Zhao, W. W. Xu, Y. F. Dong, R. Xia, F. N. Liu, L. He, Q. L. Wei, M. Y. Yan, L. Q. Mai, *Phys. Chem. Chem. Phys.* **2015**, *17*, 7619.
- [14] S. Mohapatra, S. V. Nair, D. Santhanagopalan, A. K. Rai, *Electrochimica Acta* **2016**, *206*, 217.
- [15] Y. Y. Feng, H. J. Zhang, W. X. Li, L. Fang, Y. Wang, *J. Power Sources* **2016**, *301*, 78.
- [16] H. Wu, G. Chan, J. W. Choi, I. Ryu, Y. Yao, M. T. McDowell, S. W. Lee, A. Jackson, Y. Yang, L. B. Hu, Y. Cui, *Nat. Nanotechnol.* **2012**, *7*, 309.
- [17] Y. Yao, M. T. McDowell, I. Ryu, H. Wu, N. Liu, L. B. Hu, W. D. Nix, Y. Cui, *Nano Lett.* **2011**, *11*, 2949.
- [18] B. Wang, X. L. Li, X. F. Zhang, B. Luo, M. H. Jin, M. H. Liang, S. A. Dayeh, S. T. Picraux, L. J. Zhi, *ACS Nano* **2013**, *7*, 1437.
- [19] C. K. Chan, R. N. Patel, M. J. O'Connell, B. A. Korgel, Y. Cui, *ACS Nano* **2010**, *4*, 1443.
- [20] H. Kim, M. Seo, M. H. Park, J. Cho, *Angew. Chem., Int. Ed.* **2010**, *49*, 2146.
- [21] T. Hanrath, B. A. Korgel, *Adv. Mater.* **2003**, *15*, 437.
- [22] T. Song, J. L. Xia, J. H. Lee, D. H. Lee, M. S. Kwon, J. M. Choi, J. Wu, S. K. Doo, H. Chang, W. Park, D. S. Zang, H. S. Kim, Y. G. Huang, K. C. Hwang, J. A. Rogers, U. Paik, *Nano Lett.* **2010**, *10*, 1710.
- [23] N. Yan, F. Wang, H. Zhong, Y. Li, Y. Wang, L. Hu, Q. W. Chen, *Sci. Rep.* **2013**, *3*, 1568.
- [24] Z. Favors, W. Wang, H. H. Bay, A. George, M. Ozkan, C. S. Ozkan, *Sci. Rep.* **2014**, *4*, 4605.
- [25] B. K. Guo, J. Shu, Z. X. Wang, H. Yang, L. H. Shi, Y. N. Liu, L. Q. Chen, *Electrochem. Commun.* **2008**, *10*, 1876.
- [26] B. Gao, S. Sinha, L. Fleming, O. Zhou, *Adv. Mater.* **2001**, *13*, 816.
- [27] W. S. Chang, W. S. Chang, C. M. Park, J. H. Kim, Y. U. Kim, G. Jeong, H. J. Sohn, *Energy Environ. Sci.* **2012**, *5*, 6895.
- [28] M. Sasidharan, D. Liu, N. Gunawardhana, M. Yoshio, K. Nakashim, *J. Mater. Chem.* **2011**, *21*, 13881.
- [29] H. H. Li, X. L. Wu, H. Z. Sun, K. Wang, C. Y. Fan, L. L. Zhang, F. M. Yang, J. P. Zhang, *J. Phys. Chem. C* **2015**, *119*, 3495.
- [30] Y. R. Liang, L. F. Cai, L. Y. Chen, X. D. Lin, R. W. Fu, M. Q. Zhang, D. C. Wu, *Nanoscale* **2015**, *7*, 3971.
- [31] C. W. Wang, K. W. Liu, W. F. Chen, J. D. Zhou, H. P. Lin, C. H. Hsu, P. L. Kuo, *Inorg. Chem. Front.* **2016**, *3*, 1398.
- [32] Y. Yao, J. J. Zhang, L. G. Xue, T. Huang, A. S. Yu, *J. Power Sources* **2011**, *196*, 10240.
- [33] Q. S. Xie, Y. T. Ma, X. P. Wang, D. Q. Zeng, L. S. Wang, L. Q. Mai, D. L. Peng, *ACS Nano* **2016**, *10*, 1283.
- [34] K. Song, S. Yoo, K. Kang, H. Heo, Y.-M. Kang, M.-H. Jo, *J. Power Sources* **2013**, *229*, 229.
- [35] M. Li, J. Li, K. Li, Y. Zhao, Y. Zhang, D. Gosselink, P. Chen, *J. Power Sources* **2013**, *240*, 659.
- [36] N. Fukata, M. Mitome, Y. Bando, W. Z. Wu, Z. L. Wang, *Nano Energy* **2016**, *26*, 37.
- [37] A. M. Venezia, R. Bertonecello, G. Deganello, *Surf. Interface Anal.* **1995**, *23*, 239.

- [38] L. Zhang, J. W. Deng, L. F. Liu, W. P. Si, S. Oswald, L. X. Xi, M. Kundu, G. Z. Ma, T. Gemming, S. Baunack, F. Ding, C. L. Yan, O. G. Schmidt, *Adv. Mater.* **2014**, *26*, 4527.
- [39] H. J. Kim, S. Choi, S. J. Lee, M. W. Seo, J. G. Lee, E. Deniz, Y. J. Lee, E. K. Kim, J. W. Choi, *Nano Lett.* **2016**, *16*, 282.
- [40] S. Laruelle, S. Grugeon, P. Poizot, M. Dolle, L. Dupont, J. M. Tarascon, *J. Electrochem. Soc.* **2002**, *149*, A627.
- [41] S. Grugeon, S. Laruelle, L. Dupont, J. M. Tarascon, *Solid State Sci.* **2003**, *5*, 895.
- [42] X. L. Wu, Y. G. Guo, J. Su, J. W. Xiong, Y. L. Zhang, L. J. Wan, *Adv. Energy Mater.* **2013**, *3*, 1155.
- [43] C. J. Tang, J. Z. Sheng, C. Xu, S. M. B. Khajehbashi, X. P. Wang, P. Hu, X. J. Wei, Q. L. Wei, L. Zhou, L. Q. Mai, *J. Mater. Chem. A* **2015**, *3*, 19427.